Environ Fluid Mech (2017) 17:1207–1231
DOI 10.1007/s10652-017-9545-9

ORIGINAL ARTICLE

Migration of radioactivity in multi-fraction sediments

Vladimir Maderich[1] · Kyung Tae Jung[2] · Igor Brovchenko[1] · Kyeong Ok Kim[2]

Received: 26 March 2017 / Accepted: 4 August 2017 / Published online: 16 August 2017

Abstract A new 3D radioactivity transport model coupled with multiscale circulation and multi-fractional sediment transport modules is presented. The sediment transport module simulates the transport of a mixture of one cohesive sediment fraction and a number of fractions of non-cohesive sediments of different sizes and densities. The model of radionuclide transport describes the key transport and exchange processes in the system of water-suspended and bottom multi-fraction sediments. Two-step kinetics with two successive reversible fast and slow reactions is used in the model. A noticeable feature of the model is approximation of the sediment and contamination profiles in the bed by multiple well-mixed layers to describe the vertical migration of radioactivity within bottom sediments due to erosion/deposition, molecular diffusion and bioturbation. The model accurately reproduced a laboratory experiment on the uptake of radiocesium by lake sediments. An analytical solution describing mutual adjustment of the concentrations of radioactivity in the pore water and in the multi-fraction sediment showed that activity was redistributed between different fractions of sediments far slower than between water and the total concentration in the sediment. The extended one-layer model of bottom contamination of multi-fraction sediments was derived from a general model and compared with a multi-layer model. It was found, however, that the one-layer approximation was not capable of correctly predicting the inventory due to the fact that one-layer averaged concentration can essentially differ from the near-surface value in the multi-layer model. Radionuclide

✉ Vladimir Maderich
vladmad@gmail.com

Kyung Tae Jung
KTJung@kiost.ac

Igor Brovchenko
ibrovchenko@gmail.com

Kyeong Ok Kim
kokim@kiost.ac

[1] Institute of Mathematical Machine and System Problems, Kiev, Ukraine

[2] Korea Institute of Ocean Science and Technology, Ansan, Republic of Korea

transport in channel with bottom depression was simulated to estimate the effects of erosion/deposition and the multi-fractionality of sediments on the transport process. It was shown that these factors affect the distribution of sediments by forming local maxima and minima of activity at the beginning and end of the depression, respectively, due to the redistribution of contaminated bottom sediments by flow. The developed model can also be used to simulate the transport of a wide class of toxic substances sorbed on sediments.

Keywords Radioactivity transport · Multifraction sediments · Two-step sequential reaction kinetics · Bioturbation

List of symbols

a_{bds}	"Desorption" rate of activity from sediment layer to the water column
a_{ds}	desorption rate
a_{rs}	"Redistribution" rate of radioactivity between sediment fractions
a_{fs}	Direct exchange rate between fast and slow reversible phases of radionuclide
a_{sf}	Reverse exchange rate between fast and slow reversible phases of radionuclide
a_i	Reference level above the bottom
C_d^w	Concentration of the dissolved radionuclide in the water column
$C_{p,i}^w$	Concentration of the fast reversible radionuclide phase in i fraction of suspended sediments
$\tilde{C}_{p,i}^w$	Concentration of slow reversible radionuclide phase in i fraction of suspended sediments
C_p^w	Total concentration of radionuclide in suspended sediments
$C_{d,j}^b$	Concentration of radionuclide in the pore water
$C_{s,i,j}^b$	Concentration of fast reversible radionuclide phase in i fraction of bottom sediments
$\tilde{C}_{s,i,j}^b$	Concentration of slow reversible radionuclide phase in i fraction of bottom sediments
$\hat{C}_{s,j}^b$	Total concentration of fast reversible radionuclide phase in the bottom sediments
$\check{C}_{s,j}^b$	Total concentration of slow reversible radionuclide phase in the bottom sediments
d_i	Size of the sediment fraction i
$DIFF$	Vertical and horizontal turbulent diffusion terms
D_i	Sediment deposition flux
E_i	Sediment erosion flux
$E_{0,i}$	Sediment erosion rate
i	Notation of sediment fraction ($0 \leq i \leq n$)
j	Notation of bottom sediment layer ($1 \leq j \leq m$)
$K_{d,i}$	Distribution coefficient for one-step reaction
K_H	Horizontal eddy diffusivity
m	Total number of bottom sediment layers
n	Total number of fractions of sediment
q_i	Deposition flux of aerosoles
q_d	Atmospheric deposition flux of dissolved radionuclide
$q_{p,i}$	Atmospheric deposition flux of particulate radionuclide
Re	Reynolds number
S	Salinity

Sc	Schmidt number
$S^w_{p,i}$	Concentration of ith fraction of suspended sediment
t	Time
$\mathbf{U}$	Velocity
u_*	Friction velocity
W	Vertical velocity
$W^{(j,j+1)}_{bt}$	Bioturbation exchange velocity between sediment layers
$W_{p,i}$	Settling velocity of sediment fraction i
$W^{pw}_{(j,j+1)}$	Exchange rate between bottom sediment layers
z	Vertical coordinate
z_0	Roughness height
Z_j	Thickness of bottom sediment layer
z_{bt}	Thickness of bioturbation layer
z_{eff}	Characteristic decay scale for bioturbation
δ_*	Average height of the roughness elements
$\epsilon^w_{s,j}$	Porosity
ϵ^s_j	Solids volume fraction
η	Sea level elevation
θ	Correction factor for desorption rate
λ	Radioactivity decay constant
$\nu_{B,j}$	Bioturbation coefficient
ν_D	Free solution diffusion coefficient
ν_M	Kinematic viscosity
ν_T	Vertical eddy diffusivity
$\rho_{s,i}$	Density of ith fraction of sediment
τ_b	Bottom shear stress
τ_{cd}	Critical shear stress for the deposition of cohesive sediments
$\tau_{cr,i}$	Critical shear stress for the erosion
$\phi_{i,j}$	Volume fraction of sediment particles of ith fraction and jth layer
$\phi_{0,cr}$	Critical cohesive sediment fraction in the bed
χ	Exchange velocity
ψ^2	Tortuosity parameter

1 Introduction

An unprecedent release of radionuclides to the ocean occurred due to accident at the Fukushima Daiichi nuclear plant (FDNPP) caused by the Tohoku earthquake and the subsequent tsunami on March 11, 2011 [6]. The released radionuclides were mostly diluted and transported eastward by currents. The bottom deposits contain approximately only 1% of the released radionuclides (mostly ^{134}Cs and ^{137}Cs) [5]. However, due to the rapid dilution of radionuclides by intensive currents and eddies, the bottom sediments on the Japan shelf have become the main source of remobilization of activity to water column. Similarly, desorption from bottom sediments is the main source of dissolved ^{137}Cs in the Irish Sea following the reduction of routine release from the Sellafield reprocessing plant [19].

Radionuclides are transported in the water column in the solute and sorbed by the suspended sediments. The exchange processes with bed sediments include diffusion from the water column to the pore water of the sediment layer, sorption/desorption, erosion of bed sediment and deposition of suspended matter. The radionuclide migration in sea deposits is governed by molecular diffusion and reworking of sediments by animals (bioturbation). Continuous measurement of the radiocesium distribution on the sea floor in the vicinity of FDNPP demonstrated strong patchiness of activity [15, 37, 39]. The potential reasons include heterogeneity in the physical and chemical features of the sediments [22] and local inhomogeneities of the bottom topography resulting in variations in erosion and deposition [39]. These processes are complex and not fully understood. Table 1 shows the important features of a number of models of radioactivity transport in the marine environment. Diffusion in pore water and bioturbation of the sediments are considered in only a few models [2, 11] of the migration of sedimentary radioactivity. The continuous profile of multi-fraction sediments with inhomogeneous porosity in most of models was substituted by an averaged distribution of a single fraction of sediments. The pore water diffusion and exchange with solids was represented by the semi-empirical sorption-desorption relation for the near-bottom water concentration and concentration in the sediment layer. In common with many trace elements, radionuclide kinetics depend on the grain size. The dependence of the kinetics on the sediment size is taken into account in many models following [1] and [24, 25]. The exchange processes between water and solids in most models are described in the frame of a one-step reversible reaction of sorption/desorption on the surface of particles (e.g. [18, 26, 27]); however, the mobility of radionuclides can be affected by a slow sorption process which "fixes" the ion to the solids due to the penetration of ions into the structure of sediment particles and interlattice spacing [20, 22, 33, 35]. These processes were taken into account using two-step fast and slow reversible reactions [9, 20, 25, 36].

However, the existing models do not fully describe the complex processes of radionuclide exchange in the solute between the water column and pore water and in the solid due to the erosion/deposition and redistribution of activity between the bottom sediment fractions. The ability to use a single-layer model of bottom sediments instead of a continuously stratified layer model is also insufficiently justified. In this work, our aim is to develop a radioactivity transport model that can be coupled with a hydrodynamics model

Table 1 Models of radioactivity transport in sea

Reference	Water column transport	Sediment layer	Sediment fraction	Reaction kinetics	Pore water	Sorption dependence on particle size
[21]	3D	Single	Single	1 step	No	No
[24]	2D	Single	Single	1 step	No	Yes
[17]	3D	Single	Single	1 step	No	No
[2]	2D	Multiple	Multiple	1 step	Yes	Yes
[25]	2D	Single	Single	2 step	No	Yes
[26]	3D	Single	Multiple	1 step	No	Yes
[13]	3D	Single	Single	1 step	No	No
[11]	3D	Multiple	Single	1 step	Yes	No
This model	3D	Multiple	Multiple	2 step	Yes	Yes

and multi-fraction sediment transport and multi-layer bed model (e.g. SELFE/SCHISM [30, 32, 45, 46]). The radioactivity transport model should describe the transport, exchange processes and migration in the bed for a heterogeneous environment where the sediment characteristics (sediment fractions, densities and porosity) vary in space. The model is described in Sect. 2. The results of a comparison with laboratory experiment are shown in Sect. 3. Mutual adjustment of the concentrations of radioactivity in the pore water and in the multi-fraction sediment is studied in Sect. 4. A one-layer model of bed sediment contamination is derived from the multi-layer bed model and studied in Sect. 5. The effects of erosion and the deposition of multi-fraction sediments on radionuclide transport in channel with bottom depression are considered in Sect. 6. Conclusions are drawn in Sect. 7.

2 Model equations

2.1 Hydrodynamics model

The sediment and radionuclide transport models are embedded in the circulation modelling system SELFE/SCHISM [32, 45, 46] in which the Reynolds-averaged Navier–Stokes equations in the hydrostatic and Boussinesq approximations were closed using the generic length-scale turbulence model [40]. The detailed description of the model and methods for the numerical solution of the model equations using an unstructured grid and the finite element method can be found in [32, 46].

2.2 Multi-fraction sediment transport model

The sediment transport model is an extension of the model [30] developed for the transport of multi-fraction non-cohesive sediments. The extended model includes transport of the cohesive sediment where small particles of clay are significantly influenced by surface chemical-electrostatic effects and tend to aggregate together forming flocs in the water column and becoming compact in the bottom sediments [44]. The model simulates the transport of a mixture of one fraction of cohesive sediment ($i = 0$) and n fractions of non-cohesive sediments ($1 \leq i \leq n$) of different sizes d_i and densities $\rho_{s,i}$. The sediments are transported in the water column as suspended sediments, and mass exchange between the bottom and the water column is due to deposition and erosion. Sediment particles migrate in the bottom deposit due to bioturbation. Following [30], a continuous vertical distribution of bottom sediments was approximated as a sequence of well-mixed layers ($1 \leq j \leq m$), as shown in Fig. 1. These layers of thickness Z_j are characterized by porosity ϵ_j^w, the volume fraction of sediment particles of the ith fraction $\phi_{i,j}$ in the jth layer ($\sum_{i=0}^{n} \phi_{i,j} = 1$). Describing the deposition and erosion of the mixture of cohesive and non-cohesive sediments, we follow the assumptions [41] that these processes depend on the critical cohesive sediment fraction ($i = 0$) in the bed $\phi_{0,cr}$. The erosion of mixtures of cohesive and non-cohesive sediments is independent process for each sediment fraction in non-cohesive regime when the cohesive sediment content does not exceed critical value ($\phi_{0,1} \leq \phi_{0,cr}$), whereas in the cohesive regime ($\phi_{0,1} > \phi_{0,cr}$), the erosion of non-cohesive and cohesive sediments simultaneously occurs as cohesive sediment erosion. Deposition is an independent process for cohesive and non-cohesive sediments. The total number of layers m is constant, requiring merging or splitting of the bottom layers due to deposition and erosion

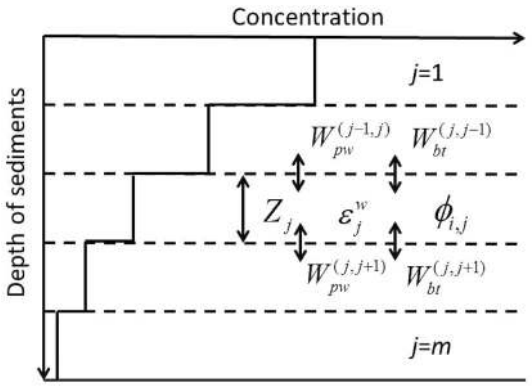

Fig. 1 Schematics of the bottom sediment layers and vertical distribution of the radioactivity concentration in the bottom

processes [43]. Bioturbation is the reworking of sediments by marine organisms. The depth of bioturbation is limited by the availability of organic matters consumed by bioturbating organisms [8]. In general, bioturbation is three-dimensional process which can be non-local due to presence of head-down deposit feeders [7]. Here we confine ourselves to a description of the bioturbation as a diffusion-type process in vertical direction with corresponding bioturbation coefficient. Therefore the bioturbation exchange velocity $W_{bt}^{(j,j+1)}$ between sediment layers j and $j+1$ (see Fig. 1 is approximated by finite-difference representation by the bioturbation coefficients $v_{B,j}$ in the layers as

$$W_{bt}^{(j,j+1)} = \frac{2v_{B,j}v_{B,j+1}}{v_{B,j}Z_{j+1} + v_{B,j+1}Z_j}. \tag{1}$$

The vertical distribution of the bioturbation coefficient can be approximated as $v_{B,j} = v_{B,1}(1 - z_{bj}/z_{bt})^2$ where $z_{bj} = \sum_{k=1}^{j} Z_k$, z_{bt} is the thickness of the bioturbation layer [8] or $v_{B,j} = v_{B,1}\exp(-z_{bj}^2/z_{eff}^2)$, where z_{eff} is the characteristic decay scale for bioturbation. The values of $v_{B,j}$ depend on the depth and local processes, e.g. in the FDNPP area the bioturbation coefficient varies in range from 10^{-13} to 10^{-11} m^2 s^{-1} [5]. The detailed description of the sediment transport model is given in the "Appendix".

2.3 The equations of radionuclide transport

The model of radionuclide transport describes the key processes in the system of water-multi-fraction sediments (see Table 1). In the water column, radionuclides in the dissolved and particulate phases are transported by currents (advection processes) with the simultaneous influence of turbulent diffusion. The radionuclides in the dissolved phase interact with the particulate phase radionuclides in suspended sediments and bottom deposits. A transfer of activity between the dissolved and particulate phases is described by adsorption-desorption processes. The settling of contaminated suspended sediments and bottom erosion are important pathways of radionuclide exchange between the bottom and suspended sediment. The continuous vertical profile of activity in the bottom sediments was also approximated as a sequence of well-mixed layers (Fig. 1). A transfer of activity between the water column and the pore water in the bottom sediment is governed by several mechanisms: (1) bottom boundary layer turbulence regulated diffusional transfer; (2) molecular diffusion for laminar flows; (3) diffusion driven by the bioturbation; (4)

bioirrigation; (5) advection driven by surface waves; (6) advection driven by subsurface groundwater flow [7, 31]. In the model mechanisms (1)–(2) contribute in the transfer process. Following [9, 20, 26, 35] two-step kinetics with two successive reversible fast and slow reactions is used in the model (Fig. 2).

The equations for spatio-temporal variations of the concentration of the dissolved phase of radionuclide in the water column C_d^w (Bq m^{-3}) and for the concentration of fast and slow reversible radionuclide phases $C_{p,i}^w$ and $\tilde{C}_{p,i}^w$, respectively (Bq m^{-3}) for each suspended sediment size fraction i in the water column are written as

$$\frac{\partial C_d^w}{\partial t} + \mathbf{U}\nabla C_d^w = -a_{ds}\left(C_d^w \sum_{i=0}^{n} S_{p,i}^w K_{d,i} - C_p^w\right) - \lambda C_d^w + DIFF\left(C_d^w\right), \tag{2}$$

$$\frac{\partial C_{p,i}^w}{\partial t} + \mathbf{U}\nabla C_{p,i}^w = W_{p,i}\frac{\partial C_{p,i}^w}{\partial z} + a_{ds}\left(C_d^w S_{p,i} K_{d,i} - C_{p,i}^w\right) - a_{fs} C_{p,i}^w + a_{sf}\tilde{C}_{p,i}^w - \lambda C_{p,i}^w + DIFF\left(C_{p,i}^w\right), \tag{3}$$

$$\frac{\partial \tilde{C}_{p,i}^w}{\partial t} + \mathbf{U}\nabla \tilde{C}_{p,i}^w = W_{p,i}\frac{\partial \tilde{C}_{p,i}^w}{\partial z} + a_{fs} C_{p,i}^w - a_{sf}\tilde{C}_{p,i}^w - \lambda \tilde{C}_{p,i}^w + DIFF\left(\tilde{C}_{p,i}^w\right), \tag{4}$$

where t is time; x, y, z are Cartesian coordinates; z is the vertical coordinate directed upward; $\mathbf{U} = (U, V, W)$ is the velocity; ∇ is a 3D vector operator; $S_{p,i}^w$ is the concentration of the ith fraction of suspended sediment (kg m^{-3}); $W_{p,i} > 0$ is the settling velocity of the ith sediment fraction (m s^{-1}). The term $DIFF$ presents the vertical and horizontal turbulent diffusion as

$$DIFF(\,) = \frac{\partial}{\partial z} v_T \frac{\partial(\,)}{\partial z} + \nabla_H K_H \nabla_H(\,), \tag{5}$$

where v_T and K_H are the vertical and horizontal eddy diffusivity, respectively (m^2 s^{-1}), and ∇_H is the horizontal vector operator. The phase exchange between the dissolved and fast reversible radionuclide fractions is written in terms of the desorption rate a_{ds} (s^{-1}) and

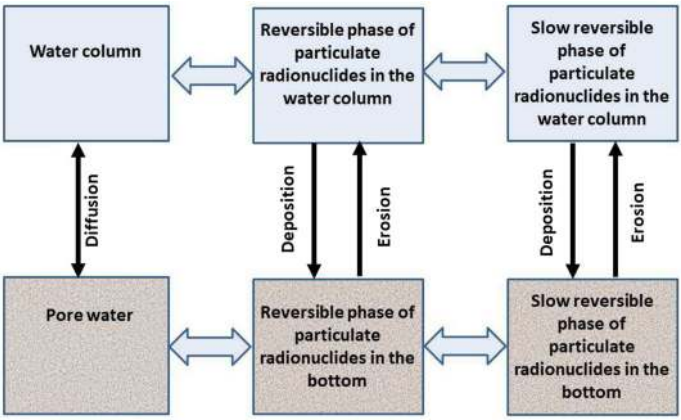

Fig. 2 Schematics of radionuclide transfer in the water column and bottom using kinetic model consisting two successive reversible fast and slow reactions

parameter $K_{d,i}$ ($m^3\ kg^{-1}$), whereas a_{fs} and a_{sf} (s^{-1}) are the direct and reverse exchange rates between the fast and slow reversible fractions of the radionuclides and λ is the decay constant. The total concentration of the fast reversible radionuclide phase in the suspended sediment (Bq m^{-3}) is

$$C_p^w = \sum_{i=1}^{n} C_{p,i}^w. \tag{6}$$

Parameter $K_{d,i}$ is the distribution coefficient for the one-step reaction [12]. The dependence of $K_{d,i}$ on the sediment particle diameter d_i is written following [24] as

$$K_{d,i} = \frac{\chi}{a_{ds}\rho_{s,i}}\frac{6}{d_i}, \tag{7}$$

where χ is the exchange velocity ($m\ s^{-1}$). The distribution coefficient for the fast reversible fraction decreases with the concentration of competitive ions in water. This effect was parameterized by [26] as a dependence on the salinity S:

$$\chi = \chi_0 \frac{S_0}{S + S_0} \tag{8}$$

where S_0 is constant, $S_0 = 45$ [16]. As found from experiments [16] a_{ds} is similar for different radionuclides. Following [26] we adopted constant value $a_{ds} = 1.16 \cdot 10^{-5}\ s^{-1}$, whereas the value of χ_0 depends on the radionuclide. According to [26] the values of χ_0 for Cs and Pu are $3.8 \cdot 10^{-6}$ and $5.21 \cdot 10^{-5}\ m\ s^{-1}$, respectively.

The total concentration of fast and slow reversible radionuclide particulate phases $\hat{C}_{s,j}^b$ and $\check{C}_{s,j}^b$ in the bottom sediment (Bq m^{-3}) are, respectively,

$$\hat{C}_{s,j}^b = \sum_{i=0}^{n} \rho_{s,i}\phi_{i,j}C_{s,i,j}^b, \quad \check{C}_{s,j}^b = \sum_{i=0}^{n} \rho_{s,i}\phi_{i,j}\tilde{C}_{s,i,j}^b \tag{9}$$

Define parameter $\hat{K}_{d,j}$ as

$$\hat{K}_{d,j} = \sum_{i=1}^{n} \rho_{s,i}\phi_{i,j}K_{d,i}. \tag{10}$$

The radioactivity in the upper bottom layer ($j = 1$) exists in three phases (Fig. 2). The equations for layer averaged concentration of radionuclide in the pore water $C_{d,1}^b$ (Bq m^{-3}), layer averaged concentrations of particulate radionuclide for each sediment fraction i in the fast reversible phase $C_{s,i,1}^b$ (Bq kg^{-1}) and slow reversible phase $\tilde{C}_{s,i,1}^b$ (Bq kg^{-1}) are written as

$$\begin{aligned}\frac{\partial Z_1 \epsilon_1^w C_{d,1}^b}{\partial t} = {} & \epsilon_1^w W_{(0,1)}^{pw}\left(C_d^w(-H) - C_{d,1}^b\right) - (W_{(1,2)}^{pw} + W_{(1,2)}^{bt})\left(\epsilon_1^w C_{d,1}^b - \epsilon_2^w C_{d,2}^b\right) \\ & - a_{ds}\theta Z_1 \epsilon_1^s\left(\hat{K}_{d,1}C_{d,1}^b - \hat{C}_{s,1}^b\right) - \lambda \epsilon_1^w Z_1 C_{d,1}^b,\end{aligned} \tag{11}$$

$$\frac{\partial Z_1 \epsilon_1^s \phi_{i,1} C_{s,i,1}^b}{\partial t} = -W_{(1,2)}^{bt}\left(\epsilon_1^s \phi_{i,1} C_{s,i,1}^b - \epsilon_2^s \phi_{i,2} C_{s,i,2}^b\right) + a_{ds}\theta \epsilon_1^s \phi_{i,1} Z_1 \left(K_{d,i} C_{d,1}^b - C_{s,i,1}^b\right) - \epsilon_1^s a_{fs} \phi_{i,1} Z_1 C_{s,i,1}^b + \epsilon_1^s a_{sf} \phi_{i,1} Z_1 \tilde{C}_{s,i,1}^b + \frac{\phi_{i,1} D_i C_{s,i}^w}{S_i \rho_{s,i}} - \frac{E_i C_{s,i,1}^b}{\rho_{s,i}} - \lambda \epsilon_1^s \phi_{i,1} Z_1 C_{s,i,1}^b, \tag{12}$$

$$\frac{\partial Z_1 \epsilon_1^s \phi_{i,1} \tilde{C}_{s,i,1}^b}{\partial t} = -W_{(1,2)}^{bt}\left(\epsilon_1^s \phi_{i,1} \tilde{C}_{s,i,1}^b - \epsilon_2^s \phi_{i,2} \tilde{C}_{s,i,2}^b\right) + \epsilon_1^s a_{fs} \phi_{i,1} Z_j C_{s,i,1}^b - \epsilon_1^s a_{sf} \phi_{i,1} Z_j \tilde{C}_{s,i,1}^b - \lambda \epsilon_1^s \phi_{i,1} Z_j \tilde{C}_{s,i,1}^b, \tag{13}$$

where D_i is the sediment deposition rate ($\mathrm{kg\,m^{-2}s^{-1}}$) and E_i is the sediment erosion rate ($\mathrm{kg\,m^{-2}s^{-1}}$). The equations for the layer-averaged concentration of radionuclide in the pore water $C_{d,j}^b$ and the concentration of fast and slow reversible radionuclide phases for each sediment size fraction $C_{s,i,j}^b$ and $\tilde{C}_{s,i,j}^b$, respectively, written for the remaining sediment layers ($1 < j \leq m$) are

$$\frac{\partial Z_j \epsilon_j^w C_{d,j}^b}{\partial t} = (W_{(j-1,j)}^{pw} + W_{(j-1,j)}^{bt})\left(\epsilon_{j-1}^w C_{d,j-1}^b - \epsilon_j^w C_{d,j}^b\right) - (W_{(j,j+1)}^{pw} + W_{(j,j+1)}^{bt})\left(\epsilon_j^w C_{d,j}^b - \epsilon_{j+1}^w C_{d,j+1}^b\right) - a_{ds}\theta Z_j \epsilon_j^s \left(C_{d,j}^b \hat{K}_{d,j} - \hat{C}_{s,j}^b\right) - \lambda \epsilon_j^w Z_j C_{d,j}^b, \tag{14}$$

$$\frac{\partial Z_j \epsilon_j^s \phi_{i,j} C_{s,i,j}^b}{\partial t} = W_{(j-1,j)}^{bt}\left(\epsilon_{j-1}^s \phi_{i,j-1} C_{s,i,j-1}^b - \epsilon_j^s \phi_{i,j} C_{s,i,j}^b\right) - W_{(j,j+1)}^{bt}\left(\epsilon_j^s \phi_{i,j} C_{s,i,j}^b - \epsilon_{j+1}^s \phi_{i,j+1} C_{s,i,j+1}^b\right) + a_{ds}\theta \epsilon_j^s \phi_{i,j} Z_j \left(K_{d,i} C_{d,j}^b - C_{s,i,j}^b\right) - a_{fs} \epsilon_j^s \phi_{i,j} Z_j C_{s,i,j}^b + a_{sf} \epsilon_j^s \phi_{i,j} Z_j \tilde{C}_{s,i,j}^b - \lambda \epsilon_j^s \phi_{i,j} Z_j C_{s,i,j}^b, \tag{15}$$

$$\frac{\partial Z_j \epsilon_j^s \phi_{i,j} \tilde{C}_{s,i,1}^b}{\partial t} = W_{(j-1,j)}^{bt}\left(\epsilon_{j-1}^s \phi_{i,j-1} \tilde{C}_{s,i,j-1}^b - \epsilon_j^s \phi_{i,j} \tilde{C}_{s,i,j}^b\right) - W_{(j,j+1)}^{bt}\left(\epsilon_j^s \phi_{i,j} \tilde{C}_{s,i,j}^b - \epsilon_{j+1}^s \phi_{i,j+1} \tilde{C}_{s,i,j+1}^b\right) + a_{fs} \epsilon_j^s \phi_{i,j} Z_j C_{s,i,1}^b - a_{sf} \epsilon_j^s \phi_{i,j} Z_j \tilde{C}_{s,i,1}^b - \lambda \epsilon_j^s \phi_{i,j} Z_j \tilde{C}_{s,i,1}^b, \tag{16}$$

where $\epsilon_j^s = 1 - \epsilon_j^w$ is the solids volume fraction, and θ is the correction factor for the desorption rate, which takes into account that in the bed layers, a portion of the sediment particles may be hidden by other sediment particles [26]. This parameter is related to the porosity, however, there are not corresponding experiments. We adopted value $\theta = 0.1$ from [26] where it was estimated by calibration. Notice that exchange between layers for the pore water includes a bioturbation component because bioturbation enhances pore water diffusion due to particle mixing.

The boundary conditions for (2)–(4) at the free surface $z = \eta$ are:

$$v_T \frac{\partial C_d^w}{\partial z} - W C_d^w = q_d, \tag{17}$$

$$v_T \frac{\partial C^w_{p,i}}{\partial z} - (W - W_{p,i}) C^w_{p,i} = q_{p,i}, \tag{18}$$

$$v_T \frac{\partial \tilde{C}^w_{p,i}}{\partial z} - (W - W_{p,i}) \tilde{C}^w_{p,i} = \tilde{q}_{p,i}, \tag{19}$$

where η is sea level elevation, and q_d, $q_{p,i}$, $\tilde{q}_{p,i}$ are the atmospheric deposition fluxes (Bq $m^{-2}s^{-1}$) of dissolved radionuclide and particulate fast and slow phases of radionuclides, respectively. The fluxes into the bottom at $z = -H$ are

$$v_T \frac{\partial C^w_d}{\partial z} = \varepsilon_1 W^{pw}_{(0,1)} \left(C^w_d - C^b_{d,1} \right), \tag{20}$$

$$v_T \frac{\partial C^w_{p,i}}{\partial z} + W_{p,i} C^w_{p,i} = \frac{C^w_{p,i} D_i}{S_i} - C^b_{s,i} E_i, \tag{21}$$

$$v_T \frac{\partial \tilde{C}^w_{p,i}}{\partial z} + W_{p,i} \tilde{C}^w_{p,i} = \frac{\tilde{C}^w_{p,i} D_i}{S_i} - \tilde{C}^b_{s,i} E_i. \tag{22}$$

Unlike other radioactivity transport models [2, 11], the exchange rate $W^{pw}_{(0,1)}$ (mass transfer coefficient [7]) is estimated by boundary layer theory [34] and corrected for surface roughness [10] as

$$W^{pw}_{(0,1)} = 0.1778 u_* \mathrm{Re}^{-0.2} \mathrm{Sc}^{-0.604}, \tag{23}$$

where u_* is the friction velocity ($m\,s^{-1}$), $\mathrm{Re} = u_* \delta_* v_M^{-1}$ is the Reynolds number, $\mathrm{Sc} = v_M / v_D$ is the Schmidt number, v_M is the kinematic viscosity ($m^2\,s^{-1}$), v_D is the free solution diffusion coefficient ($m^2\,s^{-1}$), and δ_* is the average height of the roughness elements (m).

The exchange rate $W^{pw}_{(j,j+1)}$ between the bottom sediment layers at $j \geq 1$ is written as

$$W^{pw}_{(j,j+1)} = \frac{2 v'_{D,j} v'_{D,j+1}}{v'_{D,j} Z_{j+1} + v'_{D,j+1} Z_j}, \tag{24}$$

where the effective diffusion coefficient $v'_{D,j} = v_D \psi_j^{-2}$ is a free solution diffusion coefficient corrected for tortuosity in the sediments. The tortuosity parameter ψ_j^2 is related to the porosity following [7] as $\psi_j^2 = 1 - 2 \ln \epsilon^w_j$.

3 Model comparison with the laboratory experiment

The model was compared with a laboratory experiment [36] on the uptake of radiocesium by lake sediments. In this experiment, a plastic core tube with sediment from the lake was used. The water level was 2 cm above the sediment core of length 10 cm in the core tube of 6.9 cm diameter. At the beginning of the experiment, 10 kBq of ^{134}Cs was added to the water layer. After each incubation period, sections of the core were removed, and the concentrations of ^{134}Cs in the pore water and sediment were measured. The model simulation was conducted for a one-dimensional configuration with 1 mm resolution, where the upper 2 cm layer was filled with water. The simulation parameters were chosen

following [36] as: one-fraction ($\phi_{1,j} = 1$) sediment of size $d_1 = 100\,\mu\text{m}$ with porosity $\epsilon_j^w = 0.93$, density $\rho_{s,j} = 1442$ kg m^{-3}, diffusion coefficient $v_D = 1.45 \cdot 10^{-9}$ m^2 s^{-1}, $K_{d,1} = 2$ m^3 kg^{-1} and $a_{ds} = 1.16 \cdot 10^{-5}$ s^{-1}. According to [36], the fast reversible part of ^{134}Cs in this experiment was 0.65 after one year incubation period. The kinetic constants a_{fs} and a_{sf} were calibrated as $a_{fs} = 0.25 \cdot 10^{-7}$ s^{-1} and $a_{sf} = 0.25 \cdot 10^{-8}$ s^{-1}. The decay constant for ^{134}Cs is $\lambda = 1.06 \cdot 10^{-8}$ s^{-1}. The calculated change in the overlaying water layer ^{134}Cs concentration and profiles of the total ^{134}Cs concentration in the solid phase of the sediments $C^b_{tot,j} = C^b_{s,1,j} + \tilde{C}^b_{s,1,j}$ and in the pore water $C^b_{d,j}$ for different incubation times are compared with the measurements in Figs. 3 and 4. The geometric mean of the measured-to-simulated ratios for the total concentration in the solid phase is 0.92, with a geometric standard deviation of 1.74 for a total number of measurements $N = 30$. These estimates indicate that the model tends to slightly underpredict experimental values and that the predicted concentrations range within a factor of 2 of the measured concentrations. The results of simulation using 1-step model are also shown in these figures. As seen in Figs. 3 and 4 the 2-step model better describe experimental profiles of total ^{134}Cs concentration and concentration of ^{134}Cs in overlaying water layer for time scales greater than months.

4 Mutual adjustment of the concentrations of radioactivity in the pore water and in the multi-fraction sediment

Consider in more detail the influence of the multi-fractionality of sediments on the mutual adjustment of the concentrations of radioactivity in the pore water and in the sediment. The fast exchange processes are only considered ($a_{fs} = a_{sf} = 0$) in an isolated single multi-fraction sediment layer ($j = 1$; $W^{pw}_{(0,1)} = W^{pw}_{(1,2)} = W^{bt}_{(1,2)} = E_i = D_i = 0$) for $\lambda = 0$ to exclude diffusion, bioturbation, erosion and deposition. The solutions of the Eqs. (11)–(12) using initial conditions at $t = 0$ with $C^b_{d,1} = C^b_{d,1}(0)$, $C^b_{s,i,1} = C^b_{s,i,1}(0)$ are:

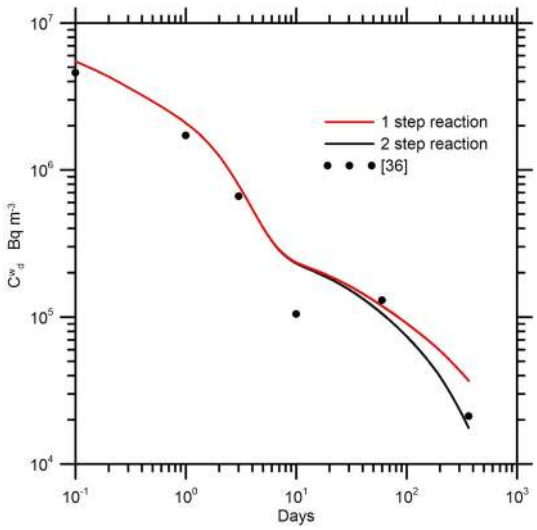

Fig. 3 Computed change of ^{134}Cs concentration in the overlaying water layer versus measurements [36]

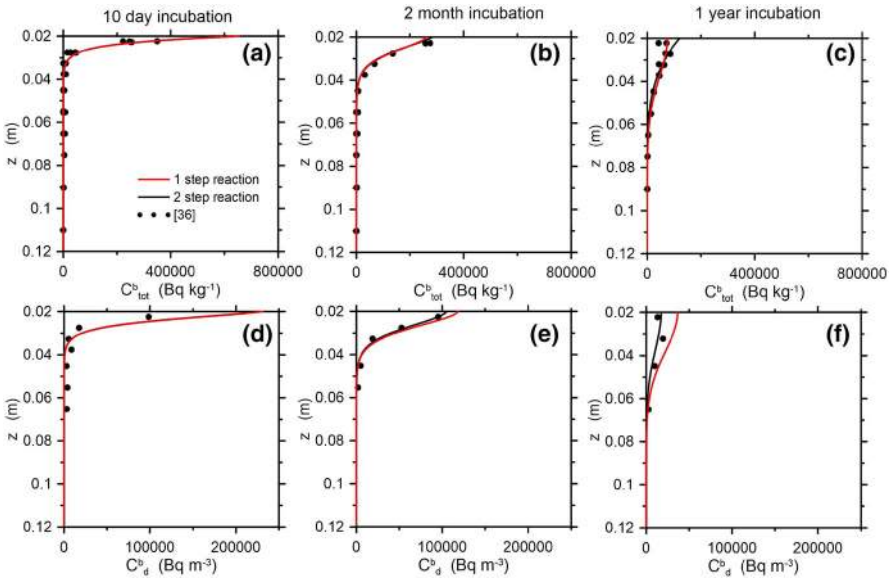

Fig. 4 Computed profiles of the total ^{134}Cs concentration in the solid phase of sediments C^b_{tot} **a–c** and in the pore water C^b_d **d–f** versus measurements [36] for different incubation times. The *red* and *black lines* represent results of simulations using 1-step and 2-step reaction models, respectively. Symbols show experiment [36] data

$$C^b_{d,1}(t) = \frac{\sigma_1}{\beta\sigma_1 + 1}\left[\beta C^b_{d,1}(0) - C^b_{s,1}(0)\right]e^{-a_{ds}\theta(\beta\sigma_1+1)t} + \frac{1}{\beta\sigma_1 + 1}\left[C^b_{d,1}(0) + \sigma_1 C^b_{s,1}(0)\right], \tag{25}$$

$$\rho_{s,i}\phi_{i,1}C^b_{s,i,1}(t) = -\frac{\beta_i}{(\beta\sigma_1 + 1)\beta}\left[\beta C^b_{d,1}(0) - \hat{C}^b_{s,1}(0)\right]e^{-a_{ds}\theta(\beta\sigma_1+1)t} + \left[\rho_{s,i}\phi_i C^b_{s,i,1}(0) - \frac{\beta_i}{\beta}\hat{C}^b_{s,1}(0)\right]e^{-a_{ds}\theta t} + \frac{\beta_i}{(\beta\sigma_1 + 1)}\left[C^b_{d,1}(0) + \sigma_1\hat{C}^b_{s,1}(0)\right], \tag{26}$$

where $\beta_i = \rho_{s,i}\phi_{i,1}K_{d,i}$, $\beta = \hat{K}_{d,1}$, $\sigma_1 = \epsilon^s_1/\epsilon^w_1$.

The difference between the concentration of radioactivity in the sediment fraction $C^b_{s,i,1}$ and the total concentration in the sediment $\hat{C}^b_{s,1}$ is

$$\rho_{s,i}\phi_{i,1}C^b_{s,i,1} - \frac{\beta_i}{\beta}\hat{C}^b_{s,1} = \left(\rho_{s,i}\phi_{i,1}C^b_{s,i,1}(0) - \frac{\beta_i}{\beta}\hat{C}^b_{s,1}(0)\right)e^{-a_{ds}\theta t}. \tag{27}$$

The solutions (25)–(26) indicate that the concentration of activity in the pore water $C^b_{d,1}$ tends toward equilibrium with the total concentration in the sediment $\hat{C}^b_{s,1}$:

$$\hat{K}^b_{d,1}C^b_{d,1} = \hat{C}^b_{s,1}. \tag{28}$$

As follows from (26) and (27), the characteristic transition time to equilibrium (28) $\sim (a_{ds}\theta\rho_{s,i}\phi_{i,1}K^b_{d,i}\epsilon^w_1/\epsilon^s_1)^{-1}$ depends on the fractional composition of the sediments,

density, porosity of sediments and kinetics of the radionuclide. This time is of several minutes for characteristic values of $\rho_{s,1} = 2.6 \cdot 10^3$ kg m^{-3}, $\epsilon_1^w = 0.6$, $\theta = 0.1$, $\phi_{1,1} = 1$ and distribution coefficient $K_{d,1}^b = 2$ m^3 kg^{-1} for ^{137}Cs, which imposes restrictions on the time step in the numerical integration of (11)–(16) for a long time. The original system of equations for a one-fraction sediment can be simplified when (28) is used and the equations for the concentration of radioactivity in the pore water and sediment are combined into a single equation for the aqueous-reversible phase $C_{e,j}^b = \epsilon_j^w C_{d,j}^b + \epsilon_j^s \hat{C}_{s,j}^b$ (e.g. [35]). However, as follows from (27), the transition time to the equilibrium state (28) of contamination of multi-fraction sediment $\sim a_{ds}^{-1}\theta^{-1}$ is on the order of 10^6 s (10 days), i.e., activity is redistributed between different fractions of sediments far slower than between water and the total concentration in the sediment. Additionally, the transfer of activity due to diffusion and/or bioturbation can also lead to a deviation from the equilibrium approximation (28). As seen in Fig. 5, the ratio of ^{134}Cs concentration of fast reversible phase to the concentration in pore water C_s^b/C_d^b slowly approaches to the constant value K_d in the simulation of experiment [36]. Therefore, for short-term processes (less than 10 days) the equilibrium assumption for reversible phase (28) is correct only for the total concentration of radioactivity in multi-fraction bottom sediments. For the sediment fraction this assumption can be used for slow long-term processes (including also the slow reversible reactions with characteristic time scales $10^7 - 10^8$ s) and far from sources of activity (e.g. from interface between water and bottom sediment).

5 One-layer model of bed sediment contamination

In many models of radioactivity transport, the distribution of activity in sediments is approximated using one layer (see Table 1). Taking into account the fact that the transitional time for the pore water concentration to reach equilibrium with the sediment is much

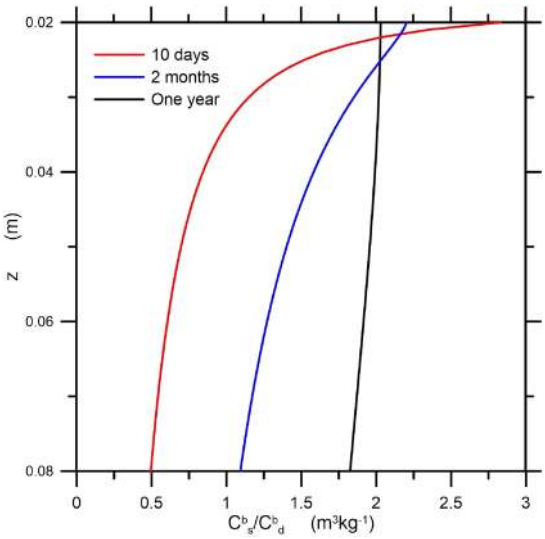

Fig. 5 The profiles of the ratio C_s^b/C_d^b computed to simulate experiment [36] for different times of incubation

less than the remaining time scales, the simplification of the one-layer Eqs. (11)–(13) for $W^{pw}_{(1,2)} = W^{bt}_{(1,2)} = 0$ can be performed assuming that exchange of the sediment pore water with the water column in (11) is balanced by redistribution of the activity in the bottom sediments. Then, the pore water concentration for the upper layer of the sediment can be obtained as

$$C^b_d = \frac{W^{pw}_{(0,1)} C^w_d(-H) + a_{ds}\theta Z_1 \sigma_1 \hat{C}^b_{s,1}}{W^{pw}_{(0,1)} + a_{ds}\theta Z_1 \sigma_1 \hat{K}^b_{d,1}}. \tag{29}$$

Using (29), the Eqs. (12)–(13) can be rewritten as

$$\frac{\partial \epsilon^s_1 \phi_{i,1} Z_1 C^b_{s,i,1}}{\partial t} = a_{bds}\epsilon^s_1 \phi_{i,1} Z_1 \left(C^w_d(-H) K^b_{d,1} - C^b_{s,i,1} \right) + a_{rs}\epsilon^s_1 \phi_{i,1} Z_1 \left(\hat{C}^b_s \frac{K^b_{d,i}}{\hat{K}^b_{d,1}} - C^b_{s,i,1} \right) + \frac{\phi_{i,1} D_i C^w_{s,i}}{S_i} - \frac{E_i C^b_{s,i,1}}{\rho_{s,i}} - \epsilon^s_1 \phi_{i,1} Z_1 (a_{fs} C^b_{s,i,1} - a_{sf} \tilde{C}^b_{s,i,1} + \lambda C^b_{s,i,1}), \tag{30}$$

$$\frac{\partial Z_1 \epsilon^s_1 \phi_{i,1} \tilde{C}^b_{s,i,1}}{\partial t} = \epsilon^s_1 \phi_{i,1} Z_1 (a_{fs} C^b_{s,i,1} - a_{sf} \tilde{C}^b_{s,i,1} - \lambda \tilde{C}^b_{s,i,1}), \tag{31}$$

where

$$a_{bds} = \frac{a_{ds}\theta W^{pw}_{(0,1)}}{W^{pw}_{(0,1)} + a_{ds}\theta Z_1 \sigma_1 \hat{K}^b_{d,1}}, \tag{32}$$

$$a_{rs} = \frac{a^2_{ds}\theta^2 Z^2_1 \sigma_1 \hat{K}^b_{d,1}}{W^{pw}_{(0,1)} + a_{ds}\theta Z_1 \sigma_1 \hat{K}^b_{d,1}}. \tag{33}$$

The Eqs. (30) and (31) extend the one-layer models (e.g. [13, 17, 21, 25, 26]) for the case of multi-fractionality and 2-step kinetics. Here, a_{bds} is the "desorption" rate of activity from the sediment layer to the water column and a_{rs} is the "redistribution" rate of radioactivity between sediment fractions. Unlike (32), the parameter corresponding to a_{bds} in [13, 17, 21, 25, 26] is empirical and, in particular, does not depend on the layer thickness, exchange rate with the water column, porosity, fraction distribution and kinetics parameters. The characteristic value of $W^{pw}_{(0,1)}$ is in the range of $10^{-6}-10^{-5}$ m s^{-1} for u_* between 0.001 and 0.01 m s^{-1} and Sc $= 10^3$. The second term in the denominator of relations (32) and (33) is much greater than the first term for characteristic values of $\rho_{s,i} \sim 10^3$ kg m^{-3}, $\varepsilon_1 \sim 1$, $\hat{K}^b_{d,1} \sim 1000, Z_1 \sim 10^{-2}$ m. The ratio $W^{pw}_{(0,1)}/(a_{ds}\theta Z_1 \sigma_1 \hat{K}^b_{d,1})$ is then of the order $10^{-2}-10^{-1}$. In that case, the parameters a_{bds} and a_{rs} can be approximated as

$$a_{bds} = \frac{W^{pw}_{(0,1)}}{Z_1 \rho^{(1)}_s \sigma_1 \hat{K}^b_{d,1}}, \; a_{rs} = a_{ds}\theta. \tag{34}$$

It is important that the value of a_{bds} in (34) is regulated by both diffusion flux from the water column and by sorption in the sediment layer. In contrast, the desorption rate a_{ds} in (34) does not affect the exchange between the water column and the sediment layer. This is

not so for a very thin layer and for strong turbulence in the water or for a small distribution coefficient (see (32)). The desorption rate a_{ds} in the one-layer model is important for the redistribution of activity between different fractions of sediment regulated by parameter a_{rs}.

Consider the idealized case of contamination of a single sediment layer by water through a diffusion mechanism. The Eqs. (30) and (31) for $E_i = D_i = \lambda = 0$ and constant values of $Z_1, \epsilon_1^w, \phi_{i,1}$ are rewritten as

$$\frac{\partial C^b_{s,i,1}}{\partial t} = a_{bds}\left(K^b_{d,i,1} C^w_d(-H) - C^b_{s,i,1}\right) + a_{rs}\left(\hat{C}^b_s \frac{K^b_{d,i}}{\hat{K}^b_{d,1}} - C^b_{s,i,1}\right) - a_{fs} C^b_{s,i,1} + a_{sf}\tilde{C}^b_{s,i,1}, \tag{35}$$

$$\frac{\partial \tilde{C}^b_{s,i,1}}{\partial t} = a_{fs} C^b_{s,i,1} - a_{sf}\tilde{C}^b_{s,i,1}. \tag{36}$$

The concentration of activity in water is prescribed to emulate accidental release and further cleaning of the contaminated bottom:

$$C^w_d(-H) = C_0 \quad \text{for } 0 \le t \le t_1, \qquad C^w_d(-H) = 0 \quad \text{for } t_1 \le t, \tag{37}$$

where C_0 and t_1 are constants. The initial values of $C^b_{s,i,1}$ and $\tilde{C}^b_{s,i,1}$ are $C^b_{s,i,1} = \tilde{C}^b_{s,i,1} = 0$ at $t = 0$. The solution of the system of Eqs. (35)–(36) is

$$\hat{C}^b_{s,1}(t) = A\exp(k_1 t) + B\exp(k_2 t) + C, \tag{38}$$

$$\begin{aligned} \check{C}^b_{s,1}(t) &= A\frac{k_1 + a_{bds} + a_{fs}}{a_{sf}}\exp(k_1 t) + B\frac{k_2 + a_{bds} + a_{fs}}{a_{sf}}\exp(k_2 t) + \frac{a_{fs}}{a_{sf}} C, \\ \rho_{s,i}\phi_{i,1} C^b_{s,i,1} &= \frac{\beta_i}{\beta}\hat{C}^b_{s,1}, \quad \rho_{s,i}\phi_{i,1}\tilde{C}^b_{s,i,1}\phi_{i,1} = \frac{\beta_i}{\beta}\check{C}^b_{s,i,1}, \end{aligned} \tag{39}$$

where $k_{1,2}$ are the roots of the quadratic characteristic equation

$$k_{1,2} = -\frac{1}{2}(a_{bds} + a_{fs} + a_{sf}) \pm \sqrt{\frac{1}{4}(a_{bds} + a_{fs} + a_{sf})^2 - a_{bds}a_{sf}}. \tag{40}$$

The roots of (40) are approximately $k_1 \approx a_{bds}$ and $k_2 \approx a_{fs}$ when $a_{bds} \gg a_{fs} \gg a_{fs}$. The solution constants are:

$$\begin{cases} \begin{cases} A = K^b_{d,1} C_0\left(1 - \dfrac{k_1 + a_{bds}}{k_1 - k_2}\right); \\ B = -K^b_{d,1} C_0 \dfrac{k_1 + a_{bds}}{k_1 - k_2}; \quad C = K^b_{d,1} C_0 \end{cases} & 0 \le t \le t_1, \\ \begin{cases} A = C^b_{s,1}(t_1) - B; \\ B = \dfrac{(k_1 + a_{bds} + a_{fs})C^b_{s,1}(t_1) - a_{sf}\tilde{C}^b_{s,1}(t_1)}{k_1 - k_2}; \quad C = 0 \end{cases} & t_1 \le t, \end{cases} \tag{41}$$

Notice that the activity according to (39) is redistributed between the sediment fractions in the equilibrium state due to the particular choice of the clean initial state.

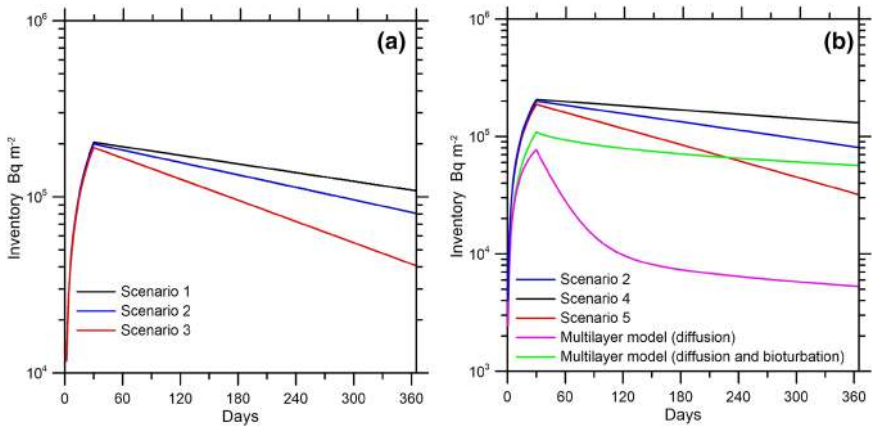

Fig. 6 The inventory variation calculated for one-layer cases 1–3 (**a**); for cases 4–5 and for the multi-layer model (**b**)

Table 2 Parameters of scenarios

Parameters	Scenario 1	Scenario 2	Scenario 3	Scenario 4	Scenario 5
$\phi_{1,1}$	0.67	0.33	0.0	0.33	0.33
$\phi_{2,1}$	0.33	0.33	0.33	0.33	0.33
$\phi_{3,1}$	0.0	0.33	0.67	0.33	0.33
Z_1 (m)	0.05	0.05	0.05	0.1	0.025
$\hat{K}_{d,1}$	7398	6425	3699	6425	6425
a_{bds} (s^{-1})	$2.17 \cdot 10^{-8}$	$5.31 \cdot 10^{-8}$	$3.12 \cdot 10^{-8}$	$1.58 \cdot 10^{-8}$	$6.07 \cdot 10^{-8}$

Figure 6 shows the dependence of the inventory $I = \sum_{j=1}^{m} \hat{C}_j^b Z_j$ on the sediment fractions (a) and the thickness of the layer (b). Three fractions of sediment sizes $R = 50$; 100 and 200 μm were considered. The corresponding fraction values $\phi_{i,1}$ are given in Table 2, together with Z_1 and the calculated values of $\hat{K}_{d,1}^b$ and a_{bds}. One-step kinetics is considered. The remaining parameters are: $\rho_{s,i} = 2600$ kg m^{-3}, $\epsilon_1^w = 0.6$, $\theta = 0.1$ and salinity $S = 34.5$. The contamination by ^{137}Cs was modelled using $\chi_0 = 3.8 \cdot 10^{-6}$ m s^{-1} and $a_{ds} = 1.16 \cdot 10^{-5}$ s^{-1}. The concentration of ^{137}Cs in water was prescribed as $C_0 = 20,000$ Bq m^{-3} in the initial period $t_1 = 30$ days. In runs 1–3, the composition of the sediments was varied to estimate the effect of the sorption-desorption process. The results of the simulation in Fig. 6 showed that the initial increase of the ^{137}Cs inventory and the concentration are almost independent of the composition of the sediment. This results can be explained by the fact that the roots (40) are approximately $k_1 \approx a_{bds}$ and $k_2 \approx 0$. Therefore, the dependence on $\hat{K}_{d,1}^b$ in the first term of the solution (38) disappears at $a_{bds}t \ll 1$. However, the decay of activity in the sediment layer essentially depends on the composition of sediment through the $\hat{K}_{d,1}^b$ values. The activity decays slower when the fraction of fine sediment is greater.

The Fig. 6b shows that decrease of sediment inventory is faster for thinner layers. Furthermore, comparison with the multi-layer model ($Z_j = 0.002$ m, $m = 120$, $\nu_D = 1.45 \cdot 10^{-9}$ m^2 s^{-1}, $\nu_{B,j} = 1 \cdot 10^{-11}$m^2 s^{-1}) in Fig. 6b shows that the inventory maximum for the multi-layer model runs is several times less than that of the single layer maximum. This result is due to the relatively slow process of diffusional transfer through the bed layers, which results in a higher concentration in the upper layer and less intensive flux of activity from water. The transfer of activity to water for $t > t_1$ in Fig. 6b differs from the single-layer model for the same reasons. Therefore, the one-layer approximation was not capable of correctly predicting the bottom sediment inventory. The bioturbation of sediments results in deepening of the contaminated layer compared with pure diffusion. As seen in Fig. 6b, this leads to greater inventory and lower exchange with the water column at $t > t_1$. These conclusions agree with the suggestion of [6] that bioturbation may provide a continuing source of Fukushima Daiichi derived ^{137}Cs contamination at the sediment-water interface over long timescales. However, for long timescales, slow reversible reactions in the sediments need to be considered [22].

6 Radionuclide transport in a channel with bottom depression

Measurements on the shelf area around the FDNPP [3, 39] showed strong heterogeneity in the distribution of the radiocesium on seafloor after the Fukushima accident. It can be the result of both local heterogeneities of sediment features [11] and the bottom topography [39]. To separate the topography effect from the effects of transport, erosion and deposition of contaminated sediments on the exchange of activity between the seafloor and water, consider the idealized case of a straight channel with a bottom depression (Fig. 7). The simulations were conducted using a hydrodynamics model [32] coupled with sediment and radioactivity transport models. The $k - kl$ model of turbulence was used. The total length of channel is 40 km, the width is 1 km, and the depth is 10 m. The length of smooth bottom depression is 4 km, and the maximum embedment is 10 m. In the first two numerical experiments (exp. 1 and exp. 2), the bottom was covered by a single-fraction sediment (sand) with grain density $\rho_{s,1} = 2600$ kg m^{-3}, size $d_1 = 150\mu$m and porosity $\epsilon_1^w = 0.6$. The roughness height z_0 was 10^{-3} m. Steady non-stratified flow with velocity 0.4 m s^{-1} and salinity $S = 34.5$ was prescribed at the left entrance of the channel. The free-slip condition on the side walls and free-outflow conditions were used. The horizontal resolution in the finite-element discretization was 50 m, 21 sigma levels were used for the water column and 25 layers of initial thickness of 0.5 cm were used for the bed sediment.

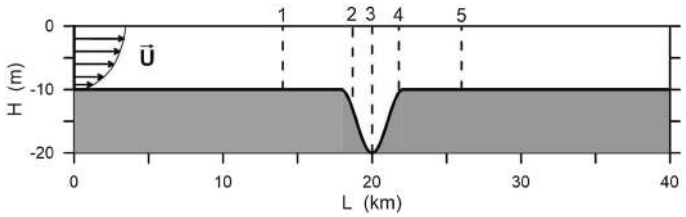

Fig. 7 Schematics of a channel with depression. *Dashed vertical lines 1–5* show the locations of the vertical profiles of ^{137}Cs in the bottom sediments

The ^{137}Cs transport model parameters are: $\chi_0 = 3.8 \cdot 10^{-6}$ m s^{-1} and $a_{ds} = 1.16 \cdot 10^{-5}\,\mathrm{s}^{-1}$, $\theta = 0.1$, $\nu_D = 1.45 \cdot 10^{-9}\mathrm{m}^2\,\mathrm{s}^{-1}$, $\nu_{B,j} = 1 \cdot 10^{-11}\mathrm{m}^2\,\mathrm{s}^{-1}$ The simulation was started from a cold start. The suspended sediment concentration was stabilized after several days of simulation spin-up ($t_0 = 3$days). Then, at period ($t_0 \le t \le t_1$), where $t_1 = 14$days, the concentration of dissolved ^{137}Cs in the channel entrance was prescribed as 10^6 Bq m^{-3}, and after this time, at $t_1 \le t$, the concentration of ^{137}Cs in the entrance was zero. In exp. 1, the exchange of activity between the seafloor and water was by diffusion and by erosion and deposition of suspended sediment, whereas in exp. 2, the exchange of activity between the seafloor and water was due to diffusion only.

The vertical distributions of the suspended sediment concentration, concentration of ^{137}Cs in the solute C_d^w and on the suspended sediments C_p^w along the channel at time $t - t_0 = 75$ days are given in Fig. 8a–c for exp. 1. As shown in Fig. 8a, suspended sediments are concentrated in a relatively thin near-bottom layer. The decrease in velocity and shear stress in the depression results in deposition of suspended sediments on the bed surface and a very low concentration of suspended sediments. At the end of the depression, strong erosion is dominant and the layer of suspended sediments is restored. The concentration of ^{137}Cs on the suspended sediments follows the distribution of suspended solids. As seen in Fig. 8c, the main source of contamination of the water column 75 days after the initial release of activity is sedimentary radiocesium. The activity in the solute diffused from the bottom pore water and desorbed from the suspended sediments (Fig. 8b) and from the bottom sediments. Turbulent diffusion redistributes the activity in the solute over the entire water column. The concentration in the solute increased along the channel due to remobilization of activity from the bed (Fig. 8c).

In the subsequent two experiments (exp. 3 and exp. 4), the bottom of the channel was covered by a mixture of three fractions of sand of density $\rho_{s,i} = 2600$ kg m^{-3}. Fractions $i = 1; 2; 3$ are characterized by grain sizes $d_i = 120; 150; 180$ μm and volume fractions

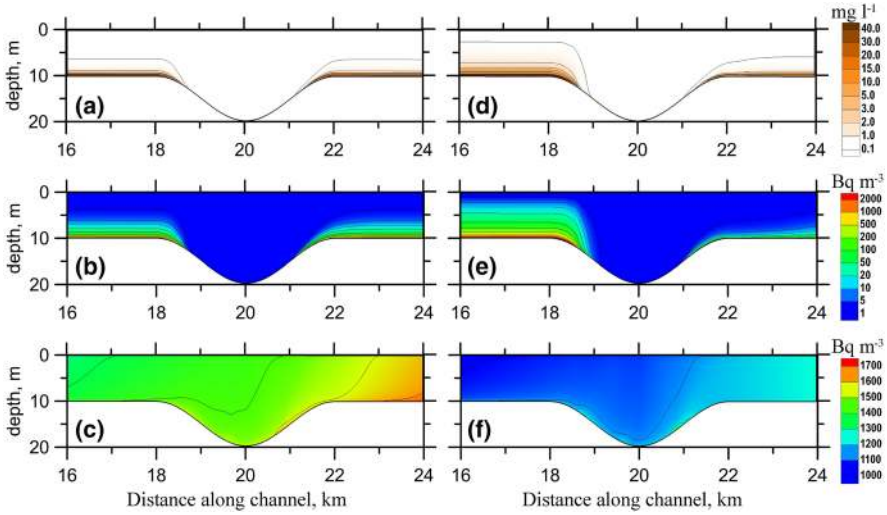

Fig. 8 The vertical sections along the channel of suspended sediment concentration S_p^w (**a**, **d**), concentration of ^{137}Cs in suspended sediments C_p^w (**b**, **e**) and in solute C_d^w (**c**, **f**) for exp. 1 (**a**–**c**) and exp. 3 (**d**–**f**) at $t - t_0 = 75$ days

$\phi_{i,1} = 0.33; 0.33; 033$, respectively. The porosity ϵ_j^w is 0.6. In exp. 3, exchange of activity between the seafloor and water occurred through diffusion and erosion and deposition of suspended sediment, whereas in exp. 4, exchange of activity between the seafloor and water was due to diffusion only. The vertical distributions of the total suspended sediment concentration, the concentration of ^{137}Cs in the solute C_d^w and on the suspended sediments C_p^w along the channel at time $t - t_0 = 75$ days for exp. 3 are given in Fig. 8d–f. The behaviour of the suspended sediments and the activity for a mixture of sediments essentially differ from the case of a single fraction of sediments. The concentration of suspended sediments in the left side of the channel in exp. 3 is much greater than that in exp. 1 (8a, d). Therefore, fine sediments clean the water, which results in a lower concentration of ^{137}Cs in the water for exp. 3 than that for exp. 1 (8c, f). In contrast, the after-depression concentration of activity on the suspended sediments for exp. 3 is lower than that for 1 because the fine fraction was washed out by erosion (8b, e).

The spatial variations of the seafloor concentration $C_{s,1}^b$ and bottom inventory are shown in Fig. 9. If only diffusion-exchange processes governed by (23) are considered (exp. 2 and 4), then $C_{s,1}^b$ decreases with increasing water column depth, as seen in Fig. 9a, due to the decreasing u_* in (23). The inventory also decreases with increasing depth (Fig. 9b) for exp. 2 and 4. Due to the particular choice of sediment fractions, $C_{s,1}^b$ and the inventory are similar in exp. 2 and 4. With time, both $C_{s,1}^b$ and the inventory monotonously decay. However, for exp. 1 and 3, sediment transport, erosion and deposition vary considerably over the seafloor depression, changing the distribution of contamination in the bottom sediments. As seen in Fig. 8b for the case of a single fraction of sediments (exp. 1), the contaminated sediments are resuspended and transported in the channel to the left edge of the bottom depression, resulting in the maximum surface concentration at $x = 18$ km. Downstream, this concentration decreases, similarly to the case without erosion/deposition; however, at the right edge of the depression, erosion results in resuspension of contaminated sediments (Fig. 9a), leading to the minimum $C_{s,1}^b$ at $x = 22$ km. As in the case without erosion and deposition, the seafloor concentration decreases with time. However, at the left edge of the bottom depression, the inventory increases permanently due to the continuing deposition of contaminated suspended sediments, whereas at the right edge, the

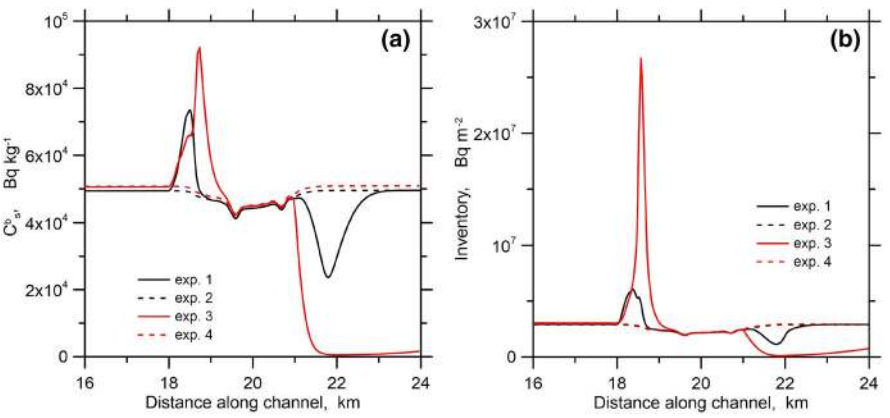

Fig. 9 The bed surface layer concentration $C_{s,1}^b$ (**a**) and inventory variation along the bottom depression (**b**) at $t - t_0 = 75$ days

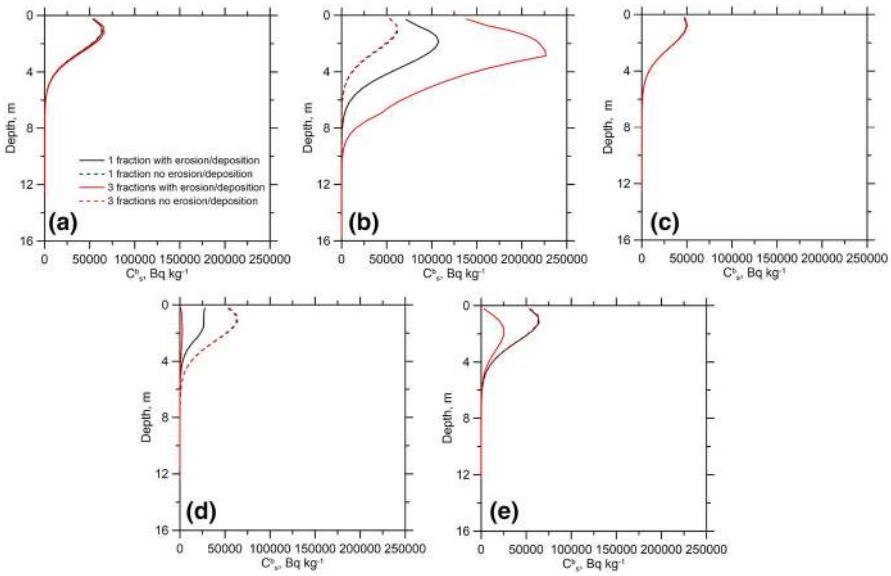

Fig. 10 The vertical profiles of the concentration of C_s^b (**a**–**e**) in locations 1–5, respectively, shown in Fig. 7

inventory decreases due to erosion. For the case of multi-fraction sediments, the maximum surface concentration appeared due to deposition of the finest fraction of sediments. The effect of deposition on the activity redistribution is much more strong, resulting in almost clean sediments at the right side of the depression.

The variation in the vertical profiles of the concentration C_s^b in the bed (Fig. 10) is shown in locations 1–5 (Fig. 7) for $t - t_0 = 75$ d for exp. 1–4. They explain the variation in the inventory along the channel (Fig. 9b). The profiles in all locations for exp. 2 and 4 are similar for these experiments, and they slightly vary along the channel. Whereas in exp. 2, the profiles in locations 1 and 5 are similar to each other and to the profiles for the case without erosion and deposition, the profiles along the depression essentially differ. The profile of the concentration in exp. 1 at the left edge of the depression (location 2) shows that this profile was formed due to the deposition of contaminated suspended sediment. The sediment profile in the center of the depression is similar to the profiles in exp. 2 and 4, demonstrating the secondary role of erosion and deposition in the depression. The profile in location 4 shows a decrease in concentration due to erosion after the initial contamination. The profiles for exp. 3 show essential changes in location 2, where deposition of fine sediments results in a high concentration of activity, in location 4, where strong erosion results in bottom cleaning, and even in location 5, where concentration is low due to the lack of transport of sediments that can deposit on the bottom.

These series of simulations indicated that erosion/deposition results in much greater effects on the inventory maximum and minimum than only diffusion exchange. The multi-fractionality of sediments and erosion/depostion give rise to the asymmetry of the inventory distribution along the symmetric depression whereas for one-fraction sediment this distribution was almost symmetric.

7 Conclusions

A new 3D radioactivity transport model coupled with multiscale circulation and multi-fractional sediment transport modules is presented. The major improvements of the model include: (1) sediment transport module simulating the transport of a mixture of one fraction of cohesive sediment and a number of fractions of non-cohesive sediments of different sizes and densities; (2) multilayer bed sediment model with varying porosity and bioturbation; (3) a model of radionuclide transport describing the key transport and exchange processes in the system of water-suspended and bottom multi-fraction sediments, including two-step kinetics with two successive reversible fast and slow reactions; (4) a noticeable feature of the model is the approximation of sediment and contamination profiles in the bed using multiple well-mixed bed layers to describe the vertical migration of the radioactivity concentration within the bottom sediments due to erosion/deposition and molecular diffusion and bioturbation.

Comparison of the model with a laboratory experiment [36] on the uptake of radiocesium by lake sediments showed good agreement. The geometric mean of the measured-to-simulated ratios for the total concentration in the solid phase was 0.92, with a geometric standard deviation of 1.74. The analytical solution describing mutual adjustment of the radioactivity concentrations in the pore water and in the multi-fraction sediment showed that the activity was redistributed between different fractions of sediments far slower (10 days for ^{137}Cs) than between water and the total concentration in the sediment (several minutes). This restricts the use of the quasi-equilibrium models (e.g. [35]) only for long-term processes of radionuclide migration in bottom sediments including also the slow reversible reactions with characteristic time scale range from months to years. We derived an extended one-layer model of bottom contamination of multi-fraction sediments from a general model, obtaining the parameter "desorption" rate of activity from the sediment layer to the water column as a function of the layer thickness and sediment properties. However, comparison of the one-layer model with the multi-layer model demonstrated that the one-layer approximation was not capable of correctly predicting the inventory due to the fact that one-layer averaged concentration can essentially differ from the near-surface value in the multi-layer model. Radionuclide transport in a channel with a bottom depression was simulated to estimate the effects of erosion/deposition and the multi-fractionality of sediments on the transport processes. It was shown that these factors affected the distribution of sediments by forming local maxima and minima of activity at the ends of the depression due to the redistribution of contaminated bottom sediments. The observed patchiness of radionuclide distribution in the bottom sediments [39] is explained by these factors.

The general conclusion from considered cases is that transport of radionuclides in the water column and their migration in sediments can be accurately described in the frame of a multi-fraction sediment transport model, multi-layer bed model and a two-step reversible sequential kinetics. Due to the model versatility it can be applied to the processes of different time and space scales from early stages of accidental releases to long-term contamination of the bottom sediments due to the regular releases. The model output provides a detailed information on 3D distribution of radionuclides in the water column and in the bed and distribution of activity in each fraction of sediments. The simplified version of a model had been used in modelling of the radionuclide dispersion after the Fukushima accident [28, 29]. The simulations of transport and migration in the bottom of ^{137}Cs after this accident using a full model with special attention to the effects of

remobilization and burial processes of activity are in progress to be presented in next paper. The developed model can also be used to simulate the transport of a wide class of toxic substances (heavy metals, organic chemicals, etc.) sorbing on sediments [38].

Acknowledgements This work was supported by KIOST major Project (PE99501), CKJORC (China–Korea Joint Ocean Research Center) Project for Nuclear Safety, State Fund for Fundamental Research of Ukraine Project 868/12879 "Transfer of radioactivity between contaminated bottom sediment and the marine environment after Fukushima and Chernobyl accidents" and IAEA Coordinated Research Project K4017. We are grateful to three anonymous reviewers for their inspiring and constructive comments, which are helpful in improving the manuscript.

Appendix

The transport equation for the concentration of the ith fraction of suspended sediment $S^w_{p,i}$ (kg m^{-3}) is

$$\frac{\partial S^w_{p,i}}{\partial t} + \mathbf{U}\nabla S^w_{p,i} = W_{p,i}\frac{\partial S^w_{p,i}}{\partial z} + DIFF\left(S^w_{p,i}\right), \tag{42}$$

The settling velocity of sediment fraction i $W_{p,i} > 0$ is calculated following [42]. For cohesive sediments $W_{p,0}$ is corrected for flocculation [44]. The boundary conditions at the free surface $z = \eta$ and at the bottom $z = -H$ are, respectively,

$$v_T\frac{\partial S^w_{p,i}}{\partial z} - (W - W_{p,i})S^w_{p,i} = q_i, \tag{43}$$

$$v_T\frac{\partial S^w_{p,i}}{\partial z} + W_{p,i}S^w_{p,i} = D_i - E_i, \tag{44}$$

where q_i is aerosol flux.

Erosion begins when the bottom shear stress τ_b exceeds some critical shear stress. The erosion flux in non-cohesive regime for ith fraction of non-cohesive sediments ($i \geq 1$) is calculated using formulations [42] as

$$E_i = E_{0,i}(d_i)\epsilon_1^s\phi_{i,1}\left(\frac{\tau_b}{\tau_{cr,i}(1+\phi_{0,1})} - 1\right)^{1.5} \quad \text{when} \quad \frac{\tau_b}{(1+\phi_{0,1})} > \tau_{cr,i}, \tag{45}$$

where $E_{0,i}(d_i) = 0.015\rho_{s,i}d_i a_i^{-1}D_{*,i}^{-0.3}$ is the erosion rate; d_i is the sediment particle diameter; $D_{*,i} = \left[g(\rho_{s,i}\rho_w^{-1} - 1)\nu_M^{-2}\right]^{1/3}$; $\tau_{cr,i}$ is the critical shear stress for sediments of fraction i; $a_i = 3d_i$ is the reference level above the bottom; ν_M is the kinematic viscosity. The critical shear stress in (45) is corrected for presence of cohesive fraction $\phi_{0,1}$ following [41]. The non-cohesive sediment flux due to sediment deposition is simulated as the flux of particles that fall with settling velocity $W_{p,i}$:

$$D_i = W_{p,i} S^w_{p,i}(-H), \tag{46}$$

where $S^w_{p,i}(-H)$ is the near-bottom concentration of suspended sediment of fraction $i > 0$. The erosion flux for cohesive sediments is described following [4] and [23] as

$$E_0 = E_{0,0}\epsilon_1^s \phi_{0,1}\left(\frac{\tau_b}{\tau_{cr,0}} - 1\right) \quad \text{when} \quad \tau_b > \tau_{cr,0}, \tag{47}$$

where $\tau_{cr,0}$ is the critical shear stress for the erosion of cohesive sediments, and $E_{0,0}$ is the erosion rate for cohesive sediments. For cohesive sediments, deposition flux appears only if the shear stress is less than the critical shear stress for deposition [14]:

$$D_0 = W_{p,0} S^w_{p,0}\left(1 - \frac{\tau_b}{\tau_{cd}}\right) \quad \text{when} \quad \tau_b < \tau_{cd}, \tag{48}$$

where τ_{cd} is the critical shear stress for the deposition of cohesive sediments. If the cohesive sediment fraction in the bed is above the critical value $\left(\phi_{0,1} > \phi_{0,cr}\right)$, then erosion for all fractions $(0 \le i \le n)$ occurs in the cohesive regime as

$$E_i = E_{0,0}\epsilon_1^s \phi_{i,1}\left(\frac{\tau_b}{\tau_{cr,0}} - 1\right) \quad \text{when} \quad \tau_b > \tau_{cr,0}. \tag{49}$$

The time variations of the thickness, sediment volume fraction and porosity in the upper sediment layer ($j = 1$) are described by equations

$$\frac{\partial Z_1}{\partial t} = \frac{1}{\epsilon_0^w}\sum_{i=0}^{n}\frac{D_i}{\rho_{s,i}} - \frac{1}{\epsilon_1^w}\sum_{i=0}^{n}\frac{E_i}{\rho_{s,i}}, \tag{50}$$

$$\frac{\partial Z_1 \epsilon_1^s \phi_{i,1}}{\partial t} = -W_{bt}^{(1,2)}\left(\phi_{i,1}\epsilon_1^s - \phi_{i,2}\epsilon_2^s\right) + (D_i - E_i)\rho_{s,i}^{-1}, \tag{51}$$

$$\frac{\partial Z_1 \epsilon_1^w}{\partial t} = -W_{bt}^{(1,2)}\left(\epsilon_1^w - \epsilon_2^w\right) + \frac{\epsilon_0^w}{\epsilon_0^s}\sum_{i=0}^{n}\frac{D_i}{\rho_{s,i}} + \frac{\epsilon_{s,1}^w}{\epsilon_1^w}\sum_{i=0}^{n}\frac{E_i}{\rho_{s,i}}. \tag{52}$$

The changes in the sediment fraction volume and porosity in the remaining layers $(2 < j \le m)$ are given by

$$\frac{\partial Z_j \phi_{i,j}\epsilon_j^s}{\partial t} = -W_{bt}^{(j,j+1)}\left(\phi_{i,j}\epsilon_j^s - \phi_{i,j+1}\epsilon_{j+1}^s\right) + W_{bt}^{(j-1,j)}\left(\phi_{i,j-1}\epsilon_{j-1}^s - \phi_{i,j}\epsilon_j^s\right), \tag{53}$$

$$\frac{\partial Z_j \epsilon_j^w}{\partial t} = -W_{bt}^{(j,j+1)}\left(\epsilon_j^w - \epsilon_{j+1}^w\right) + W_{bt}^{(j-1,j)}\left(\epsilon_{j-1}^w - \epsilon_j^w\right). \tag{54}$$

Here, ϵ_0^w and ϵ_0^s are the values for surface suspended sediments deposited on the bottom. The self-weight consolidation for cohesive sediment can be included in (50)–(54) using Gibson consolidation equations [44], however this task is out of scope of the paper.

References

1. Abril JM, Fraga E (1996) Some physical and chemical features of the variability of kd distribution coefficients of radionuclides. J Environ Radioact 30:253–270

2. Aldridge JN, Kershaw P, Brown J, McCubbin D, Leonard KS, Young EF (2003) Transport of plutonium (Pu-239/240) and caesium (Cs-137) in the Irish Sea: comparison between observations and results from sediment and contaminant transport modelling. Cont Shelf Res 23(9):869–899
3. Ambe D, Kaeriyama H, Shigenobu Y, Fujimoto K, Ono T, Sawada H, Saito H, Miki S, Setou T, Morita T, Watanabe T (2014) A high-resolved spatial distribution of radiocesium in sea sediment derived from Fukushima Dai-ichi Nuclear Power Plant. J Environ Radioact 133:264–275
4. Ariathurai CR, Arulanandan K (1978) Erosion rates of cohesive soils. J Hydraul Div 104(2):279–282
5. Black EE, Buesseler KO (2014) Spatial variability and the fate of cesium in coastal sediments near Fukushima, Japan. Biogeosciences 11:5123–5137
6. Buesseler K, Dai M, Aoyama M, Benitez-Nelson C, Charmasson S, Higley K, Maderich V, Masque P, Morris PJ, Oughton D, Smith JN (2017) Fukushima Daiichi-derived radionuclides in the ocean: transport, fate, and impacts. Ann Rev Mar Sci 9:173–203
7. Boudreau BP (1997) Diagenetic models and their implementation: modelling transport and reactions in aquatic sediments. Springer-Verlag, Berlin, Heidelberg
8. Boudreau BP (1998) Mean mixed depth of sediments: the wherefore and the why. Limnol Oceanogr 43:449–457
9. Ciffroy P, Garnier JM, Pham MK (2001) Kinetics of the adsorption and desorption of radionuclides of Co, Mn, Cs, Fe, Ag and Cd in freshwater systems: experimental and modelling approaches. J Environ Radioact 55:71–91
10. Dade WB (1993) Near-bed turbulence and hydrodynamic control of diffusional mass transfer at the sea floor. Limnol Oceanogr 38:52–69
11. Higashi H, Morino Y, Furuichi N, Ohara T (2015) Ocean dynamic processes causing spatially heterogeneous distribution of sedimentary caesium-137 massively released from the Fukushima Daiichi Nuclear Power Plant. Biogeosciences 12:7107–7128
12. IAEA (2003) Sediment distribution coefficients and concentration factors for biota in the marine environment. Technical reports series no. 422, IAEA,Vienna
13. Kobayashi T, Otosaka S, Togawa O, Hayashi K (2007) Development of a nonconservative radionuclides dispersion model in the ocean and its application to surface cesium-137 dispersion in the Irish Sea. J Nucl Sci Technol 44:238–247
14. Krone RB (1962) Flume studies of the transport of sediment in estuarial processes. Final report, Hydraulic Engineering Laboratory and Sanitary Engineering Research Laboratory, University of California, Berkeley
15. Kusakabe M, Oikawa S, Takata H, Misonoo J (2013) Spatiotemporal distributions of Fukushima-derived radionuclides in nearby marine surface sediments. Biogeoscience 10:5019–5030
16. Laissaoui A, Abril JM, Perianez R, Garca-Leon M, Garca-Montano E (1998) Determining kinetic transfer coefficients for radionuclides in estuarine waters: reference values for ^{133}Ba and effects of salinity and suspended load concentrations. J Radioanal Nucl Chem 237:55–61
17. Margvelashvily N, Maderich V, Zheleznyak M (1997) THREETOX—a computer code to simulate three-dimensional dispersion of radionuclides in stratified water bodies. Radiat Prot Dosim 73(1–4):177–180
18. Margvelashvili N, Maderich V, Yuschenko S, Zheleznyak M (2002) 3D modelling of the mud and radionuclide transport in Chernobyl cooling pond and Dnieper-Boog Estuary. In: Winterwerp JC, Kranenburg C (eds) Fine sediments dynamics in the marine environment. Proceedings of INTERCOH-2000. Elsevier, pp 595-610
19. Mitchell PI, Condren OM, Vintro LL, McMahon CA (1999) Trends in plutonium, americium and radiocaesium accumulation and long-term bioavailability in the western Irish Sea mud basin. J Environ Radioact 44:223–51
20. Nyffeler UP, Santschi PH, Li YH (1986) The relevance of scavenging kinetics to modeling of sedimentwater interactions in natural waters. Limnol Oceanogr 31:277–292
21. Onishi Y, Dummuller DC, Trent DS (1989) Preliminary testing of turbulence and radionuclide transport modeling in deep ocean environment. PNL-6853, Pacific Northwest Laboratory, Richland, Washington
22. Otosaka S, Kobayashi T (2013) Sedimentation and remobilization of radiocesium in the coastal area of Ibaraki, 70 km south of the Fukushima Dai-ichi Nuclear Power Plant. Environ Monit Assess 185:5419–5433
23. Partheniades E (1965) Erosion and deposition of cohesive soil. J Hydr Div ASCE 91:105–139
24. Periáñez R, Abril JM, Garcia-Leon M (1996) Modelling the dispersion of non-conservative radionuclides in tidal waters Part 1: conceptual and mathematical model. J Environ Radioact 31(2):127–141
25. Periáñez R (2004a) Testing the behaviour of different kinetic models for uptake/release of radionuclides between water and sediments when implemented in a marine dispersion model. J Environ Radioact 71:243–259

26. Periáñez R (2004b) The dispersion of ^{137}Cs and ^{239,240}Pu in the Rhone River plume: a numerical model. J Environ Radioact 77:301–324
27. Periáñez R, Bezhenar R, Iosjpe M, Maderich V, Nies H, Osvath I, Outola I, de With G (2015a) A comparison of marine radionuclide dispersion models for the Baltic Sea in the frame of IAEA MODARIA program. J Environ Radioact 139:66–77
28. Periáñez R, Brovchenko I, Duffa C, Jung KT, Kobayashi T, Lamego F, Maderich V, Min BI, Nies H, Osvath I, Psaltaki M, Suh K (2015b) A new comparison of marine dispersion model performances for Fukushima releases in the frame of IAEA MODARIA program. J Environ Radioact 150:247–269
29. Periáñez R, Bezhenar R, Iosjpe M, Brovchenko I, Duffa C, Jung KT, Kobayashi T, Lamego F, Maderich V, Min BI, Nies H, Osvath I, Psaltaki M, Suh K, de With G (2016) Modelling of marine radionuclide dispersion in IAEA MODARIA program: lessons learnt from the Baltic Sea and Fukushima scenarios. Sci Total Env 569–570:594–602
30. Pinto L, Fortunato AB, Zhang Y, Oliveira A, Sancho FEP (2012) Development and validation of a three-dimensional morphodynamic modelling system for non-cohesive sediments. Ocean Model 5758:1–14
31. Precht E, Huettel M (2003) Advective pore-water exchange driven by surface gravity waves and its ecological implications. Limnol Oceanogr 48(4):1674–1684
32. Roland A, Zhang Y, Wang HV, Meng Y, Teng Y, Maderich V, Brovchenko I, Dutour-Sikiric M, Zanke U (2012) A fully coupled wave-current model on unstructured grids. J Geophys Res Oceans 117:C00J33
33. Santschi PH, Honeyman BD (1989) Radionuclides in aquatic environments. Radiat Phys Chem 34:2213–2407
34. Shaw DA, Hanratty TJ (1977) Turbulent mass transfer rates to a wall for large Schmidt numbers. Am Inst Chem Eng J 23:28–37
35. Smith JT, Comans RNJ (1996) Modelling the diffusive transport and remobilisation of ^{137}Cs in sediments: the effects of sorption kinetics and reversibility. Geochim Cosmochim Acta 60:995–1004
36. Smith JT, Comans RNJ, Ireland DG, Nolana L, Hilton J (2000) Experimental and in situ study of radiocaesium transfer across the sediment-water interface and mobility in lake sediments. Appl Geochem 15:833–848
37. Sohtome T, Wada T, Mizuno T, Nemoto Y, Igarashi S, Nishimune A, Aono T, Ito Y, Kanda J, Ishimaru T (2014) Radiological impact of TEPCO's Fukushima Dai-ichi Nuclear Power Plant accident on invertebrates in the coastal benthic food web. J Environ Radioact 138:106–115
38. Thomann RV, Mueller JA (1987) Principles of surface water quality modeling and control. Harper & Row, New York 644
39. Thornton B, Ohnishi S, Ura T, Odano N, Sasaki S, Fujita T, Watanabe T, Nakata K, Ono T, Ambe D (2013) Distribution of local ^{137}Cs anomalies on the seafloor near the Fukushima Dai-Ichi Nuclear Power Plant. Mar Pollut Bull 74:344–350
40. Umlauf L, Burchard H (2003) A generic length-scale equation for geophysical turbulence models. J Mar Res 6:235–265
41. van Ledden M (2003) Sand-mud segregation in estuaries and tidal basins. Ph.D. thesis, Delft University of Technology, Delft, the Netherlands
42. van Rijn LC (1984) Sediment transport, Part II: suspended load transport. J Hydr Eng 110:1613–1641
43. Warner JC, Sherwood CR, Signell RP, Harris CK, Arango HG (2008) Development of a three-dimensional, regional, coupled wave, current, and sediment-transport model. Comput Geosci 34:1284–1306
44. Winterwerp JC, Van Kesteren WG (2004) Introduction to the physics of cohesive sediment in the marine environment, vol 56. Developments in Sedimentology Series. Elsevier, Amsterdam
45. Zhang Y, Baptista AM (2008) SELFE: a semi-implicit EulerianLagrangian finite element model for cross-scale ocean circulation. Ocean Model 21:71–96
46. Zhang YJ, Yea F, Stanev EV, Grashorn S (2016) Seamless cross-scale modelling with SCHISM. Ocean Model 102:64–81